CrossMark

Numerical study of turbulence and wave damping induced by vegetation canopies

Gangfeng Ma [a,*], James T. Kirby [b], Shih-Feng Su [c], Jens Figlus [d], Fengyan Shi [b]

[a] Department of Civil and Environmental Engineering, Old Dominion University, Norfolk, VA, USA
[b] Center for Applied Coastal Research, University of Delaware, Newark, DE, USA
[c] Department of Water Resources and Environmental Engineering, Tamkang University, Taipei, Taiwan
[d] Department of Marine Engineering Technology, Texas A & M University, Galveston, TX, USA

ARTICLE INFO

ABSTRACT

Vegetation canopies control mean and turbulent flow structure as well as surface wave processes in coastal regions. A non-hydrostatic RANS model based on NHWAVE (Ma et al., 2012) is developed to study turbulent mixing, surface wave attenuation and nearshore circulation induced by vegetation. A nonlinear $k - \varepsilon$ model accounting for vegetation-induced turbulence production is implemented to study turbulent flow within the vegetation field. The model is calibrated and validated using experimental data from vegetated open channel flow, as well as nonbreaking and breaking random wave propagation in vegetation fields. It is found that the drag-related coefficients in the $k - \varepsilon$ model C_{fk} and C_f can greatly affect turbulent flow structure, but seldom change the wave attenuation rate. The bulk drag coefficient C_D is the major parameter controlling surface wave damping by vegetation canopies. Using the empirical formula of Mendez and Losada (2004), the present model provides accurate predictions of vegetation-induced wave energy dissipation. Wave propagation through a finite patch of vegetation in the surf zone is investigated as well. It is found that the presence of a finite patch of vegetation may generate strong pressure-driven nearshore currents, with an onshore mean flow in the unvegetated zone and an offshore return flow in the vegetated zone.

Published by Elsevier B.V.

1. Introduction

Aquatic vegetation such as mangrove and seagrass is of great importance for a number of biological and physical processes in the coastal system. The most significant impact of vegetation is to increase flow resistance and reduce flow speed within the vegetation (Kadlec, 1990; Nepf, 1999; Shi et al., 1995; Wu et al., 1999), thus promoting sedimentation and the retention of suspended sediments (Lopez and Garcia, 1998; Nepf and Ghisalberti, 2008; Tsujimoto, 2000). In this sense, coastal vegetation acts as a sediment binder that resists coastal erosion. Vegetation can also dissipate wave energy (Augustin et al., 2009; Dalrymple et al., 1984; Dubi and Torum, 1997; Kobayashi et al., 1993; Li and Zhang, 2010; Lovas and Torum, 2001; Mendez and Losada, 2004; Suzuki et al., 2011) and provide significant buffering of storm surge (Loder et al., 2009; Sheng et al., 2012; Wamsley et al., 2010). More importantly, wetland vegetation can increase habitat and species diversity by introducing spatial heterogeneity to the velocity field (Shields and Rigby, 2005) and improve water quality by removing

nutrients and producing oxygen in stagnant regions (Schultz et al., 2002; Wilcock et al., 1999).

The complex array of leaves, stems, branches and other components of vegetation can tremendously alter the mean flow and turbulent mixing in vegetated aquatic environments (Jarvela, 2005; Kadlec, 1990; Nepf, 1999; Nepf and Vivoni, 2000; Shi et al., 1995). Vegetation induces additional drag on the flow field, reduces mean flow in vegetated regions, converts large-scale mean kinetic energy to small-scale turbulent kinetic energy within stem wakes, and breaks up large-scale eddies to increase turbulent dissipation (Nepf, 1999). The turbulent diffusivity within the vegetation canopy can be greatly reduced due to the downward shifting of turbulent length scale (Nepf, 1999). These processes have been extensively investigated through laboratory experiments (e.g., Ghisalberti and Nepf, 2002; Lowe et al., 2005a,b; Nepf, 1999; Nepf and Vivoni, 2000; Shi et al., 1995; Zong and Nepf, 2010, 2011). Numerical studies of vegetated open channel flow have also been conducted (e.g., Shimizu and Tsujimoto, 1994; Neary, 2003; Cui and Neary, 2008). In these studies, vegetation was ideally modeled as rigid vertical cylinders. Swaying motion as well as vortex-induced vibrations was neglected. The vegetation effects on mean flow and turbulence were accounted for through vegetation-induced drag forces. Both Reynolds-averaged Navier–Stokes simulation (RANS) and large-eddy simulation (LES) were able to capture the turbulent vegetated flow structures well.

* Corresponding author. Tel.: +1 757 683 4732; fax: +1 302 2563163.
  E-mail address: gma@odu.edu (G. Ma).

The vegetation effect on wave attenuation was observed in the field (Moller et al., 1999) and in laboratory experiments (Dubi and Torum, 1997; Lovas and Torum, 2001). Theoretical and numerical developments have also been carried out. Most of these models are based on wave energy conservation equation. For example, Kobayashi et al. (1993) derived an analytical solution for monochromatic wave attenuation by vegetation. Their analysis showed that the wave height decays exponentially in the vegetation field. Mendez and Losada (2004) developed a model for random breaking and nonbreaking wave transformation over vegetation fields. Through the calibration and verification of the model using the laboratory measurements by Dubi and Torum (1997) for nonbreaking waves and by Lovas and Torum (2001) for breaking waves, they found that the bulk drag coefficient can be parameterized as a function of the local Keulegan–Carpenter number for a specific type of plant. Suzuki et al. (2011) implemented the Mendez and Losada (2004) formulation in a full spectrum model SWAN, with an extension to include a vertical layer schematization for the vegetation. The model was shown to predict wave damping over both laboratory and field vegetation canopies reasonably well. Chen and Zhao (2012) derived two theoretical models for random wave dissipation due to vegetation, based on Hasselmann and Collins' treatment of energy dissipation and Longuet–Higgins' probability density function for joint distribution of wave height and period. Both models can reasonably predict wave height distribution over vegetation. The wave energy equation models cannot describe the instantaneous variation of the free surface. Recently, wave-resolving models have also been employed to study wave processes through vegetation patch. Augustin et al. (2009) conducted numerical studies of wave damping by emergent and near-emergent wetland vegetation using a wave-resolving nonlinear Boussinesq model COULWAVE (Lynett et al., 2002). The vegetation effect was modeled by a quadratic friction term, which was calibrated using the laboratory data. Their model could predict the instantaneous free surface damping by vegetation. However, the detailed flow structure and mixing under waves were not captured. Another type of wave-resolving model that has been recently developed in the coastal community is the nonhydrostatic wave model (Lin and Li, 2002; Ma et al., 2012; Stelling and Zijlema, 2003). The nonhydrostatic model not only predicts instantaneous free surface variation, but also captures 3D flow structures and turbulent mixing. It has also been employed to study wave–vegetation interaction by, for instance, Li and Yan (2007) and Li and Zhang (2010). In their model, turbulence was simulated by the Spalart and Allmaras (1994) turbulence model, which considers vegetation-induced turbulence production. The model was capable of predicting nonbreaking random wave damping due to vegetation. However, its capability of simulating breaking waves in the surf zone was not shown. In addition, nearshore circulation induced by the vegetation patch was not well understood.

In this paper, a new model is developed to study turbulence, wave damping as well as nearshore circulation induced by vegetation canopy. The model is based on the non-hydrostatic WAVE model (NHWAVE), which was recently developed by Ma et al. (2012). A two-equation $k − \varepsilon$ turbulence model accounting for vegetation-induced turbulence production is implemented to simulate turbulent flow within the vegetation. The model is tested against vegetated open channel flow, nonbreaking random wave dissipation over vegetation fields and vegetation-induced breaking random wave damping on a sloping beach. Then the model is employed to study nearshore currents induced by a finite patch of vegetation in the surf zone.

This paper is organized as follows. The governing equations are presented in Section 2. The nonlinear $k − \varepsilon$ model with vegetation effects are introduced in Section 3. The numerical method and boundary conditions are given in Section 4. Model calibrations and verifications as well as the model's capability to simulate breaking and nonbreaking random wave attenuation in vegetation fields are given in Sections 5 to 7. Wave propagation through a finite patch of vegetation and resulting nearshore circulation are studied in Section 8. The conclusions are finally given in Section 9.

2. Governing equations

Within the canopy, the flow moves around each stem, such that the velocity field is spatially heterogeneous at the stem scale (Nepf and Ghisalberti, 2008). A double-averaging scheme (Raupach and Shaw, 1982) is required to account for this heterogeneity. All the flow variables represented by ϕ are decomposed into time means $\overline{\phi}$ and fluctuations ϕ' as well as into their volume average $\langle \overline{\phi} \rangle$ and a departure therefrom $\overline{\phi}''$ (Raupach and Shaw, 1982). Applying this averaging scheme, the continuity and momentum equations are written as (Ayotte et al., 1999)

$$\frac{\partial \langle \overline{u}_i \rangle}{\partial x_i^*} = 0 \tag{1}$$

$$\frac{\partial \langle \overline{u}_i \rangle}{\partial t^*} + \langle \overline{u}_j \rangle \frac{\partial \langle \overline{u}_i \rangle}{\partial x_j^*} = -\frac{1}{\rho} \frac{\partial \langle \overline{p} \rangle}{\partial x_i^*} + g_i + \frac{\partial \tau_{ij}}{\partial x_j^*} + f_{Fi} + f_{Vi} \tag{2}$$

where

$$\tau_{ij} = -\langle \overline{u'_i u'_j} \rangle - \langle \overline{u}''_i \overline{u}''_j \rangle + \nu \frac{\partial \langle \overline{u} \rangle}{\partial x_j^*} \tag{3}$$

$$f_{Fi} = \frac{1}{V} \iint_{S_i} \overline{p} n_i dS \tag{4}$$

$$f_{Vi} = -\frac{\nu}{V} \iint_{S_i} \frac{\partial \overline{u}_i}{\partial n} dS \tag{5}$$

and where x_i^* is the Cartesian coordinate, $\langle \overline{u}_i \rangle$ is the double-averaged velocity component (written as $u_i = (u,v,w)$ hereafter for simplicity), ρ is water density, $\langle \overline{p} \rangle$ is double-averaged pressure, $g_i = -g\delta_{i3}$ is the gravitational body force. The kinematic momentum flux τ_{ij} includes the conventional turbulent and viscous stresses and a dispersive flux term $\langle \overline{u}''_i \overline{u}''_j \rangle$, which is negligible for uniform canopies (Ayotte et al., 1999). The viscous f_{Vi} and form drag f_{Fi} arise from the spatial perturbation of velocity and pressure, which are typically modeled together as

$$f_{di} = f_{Fi} + f_{Vi} = \frac{1}{2} C_D \lambda u_i |\mathbf{u}| \tag{6}$$

where u is the velocity vector. C_D is the drag coefficient. $\lambda = b_v N$ is the vegetation density, which is measured as frontal area per unit volume, thus having dimensions of length^{-1}. b_v is the stem size, N is the number of stems per unit area. For oscillatory flow, inertia force is not negligible and is given by

$$f_{vmi} = C_M \frac{\pi b_v^2}{4} N \frac{\partial u_i}{\partial t} \tag{7}$$

where C_M is the virtual mass coefficient.

In order to accurately represent bottom and surface geometry, a terrain-following σ-coordinate is adopted.

$$t = t^* \quad x = x^* \quad y = y^* \quad \sigma = \frac{z^* + h}{D} \tag{8}$$

where $D(x,y,t) = h(x,y) + \eta(x,y,t)$, h is water depth, η is surface elevation. Then the governing equations (Augustin et al., 2009) and (Ayotte et al., 1999) are transformed to become

$$\frac{\partial D}{\partial t} + \frac{\partial Du}{\partial x} + \frac{\partial Dv}{\partial y} + \frac{\partial \omega}{\partial \sigma} = 0 \tag{9}$$

$$\frac{\partial \mathbf{U}}{\partial t} + \frac{\partial \mathbf{F}}{\partial x} + \frac{\partial \mathbf{G}}{\partial y} + \frac{\partial \mathbf{H}}{\partial \sigma} = \mathbf{S}_h + \mathbf{S}_p + \mathbf{S}_\tau + \mathbf{S}_v \tag{10}$$

where $\mathbf{U} = (Du, Dv, Dw)^T$. The fluxes are

$$\mathbf{F} = \begin{pmatrix} Duu + \frac{1}{2}g\eta^2 + gh\eta \\ Duv \\ Duw \end{pmatrix} \quad \mathbf{G} = \begin{pmatrix} Duv \\ Dvv + \frac{1}{2}g\eta^2 + gh\eta \\ Dvw \end{pmatrix} \quad \mathbf{H} = \begin{pmatrix} u\omega \\ v\omega \\ w\omega \end{pmatrix}.$$

The source terms are given by

$$\mathbf{S}_h = \begin{pmatrix} g\eta \frac{\partial h}{\partial x} \\ g\eta \frac{\partial h}{\partial y} \\ 0 \end{pmatrix} \quad \mathbf{S}_p = \begin{pmatrix} -\frac{D}{\rho}\left(\frac{\partial p}{\partial x} + \frac{\partial p}{\partial \sigma}\frac{\partial \sigma}{\partial x^*}\right) \\ -\frac{D}{\rho}\left(\frac{\partial p}{\partial y} + \frac{\partial p}{\partial \sigma}ac\partial\sigma\partial y^*\right) \\ -\frac{1}{\rho}\frac{\partial p}{\partial \sigma} \end{pmatrix}$$

$$\mathbf{S}_\tau = \begin{pmatrix} DS_{\tau_x} \\ DS_{\tau_y} \\ DS_{\tau_z} \end{pmatrix} \quad \mathbf{S}_v = \begin{pmatrix} D(f_{dx} + f_{vmx}) \\ D(f_{dy} + f_{vmy}) \\ D(f_{dz} + f_{vmz}) \end{pmatrix}$$

where $DS_{\tau_x}, DS_{\tau_y}, DS_{\tau_z}$ are diffusion terms. The total pressure has been divided into two parts: dynamic pressure (written subsequently as p) and hydrostatic pressure $\rho g(\eta - z)$. ω is the vertical velocity in the σ coordinate image domain, given by

$$\omega = D\left(\frac{\partial \sigma}{\partial t^*} + u\frac{\partial \sigma}{\partial x^*} + v\frac{\partial \sigma}{\partial y^*} + w\frac{\partial \sigma}{\partial z^*}\right) \tag{11}$$

with

$$\begin{aligned} \frac{\partial \sigma}{\partial t^*} &= -\frac{\sigma}{D}\frac{\partial D}{\partial t} \\ \frac{\partial \sigma}{\partial x^*} &= \frac{1}{D}\frac{\partial h}{\partial x} - \frac{\sigma}{D}\frac{\partial D}{\partial x} \\ \frac{\partial \sigma}{\partial y^*} &= \frac{1}{D}\frac{\partial h}{\partial y} - \frac{\sigma}{D}\frac{\partial D}{\partial y} \\ \frac{\partial \sigma}{\partial z^*} &= \frac{1}{D}. \end{aligned} \tag{12}$$

Equations (Gottlieb et al., 2001) and (Harten et al., 1983) are well balanced such that the flux and source terms can be automatically balanced at the discrete level in the steady state (Liang and Marche, 2009).

3. Turbulence model

Various turbulence models have been used to study vegetated open channel flows, for instance, $k - \varepsilon$ models (King et al., 2012; Lopez and Garcia, 1998; Shimizu and Tsujimoto, 1994); $k - \omega$ models (Neary, 2003) and LES models (Cui and Neary, 2008). For wave–vegetation interaction, Li and Yan (2007) and Li and Zhang (2010) employed the Spalart and Allmaras (1994) turbulence model, which has been shown to be capable of simulating hydrodynamics and mixing in vegetation fields under nonbreaking waves. However, vegetated flows under breaking waves were not studied. Wave breaking is a complicated flow phenomenon, which involves the generation of intense turbulence and coherent flow structures. Lin and Liu (1998a,b) have developed a nonlinear $k - \varepsilon$ turbulence model, and successfully used it to study breaking waves on a sloping beach. Ma et al. (2011) implemented the same model into TRUCHAS (http://telluride.lanl.gov/) for the study of bubble entrainment under surf zone breaking waves. In this study, the nonlinear $k - \varepsilon$ model (Lin and Liu, 1998a,b) was

implemented into NHWAVE to simulate turbulent flow. The turbulent eddy viscosity is calculated by

$$\nu_t = C_\mu \frac{k^2}{\epsilon.} \tag{13}$$

Considering vegetation effects, the $k - \varepsilon$ equations in the conservative form are given by

$$\frac{\partial Dk}{\partial t} + \nabla \cdot (D\mathbf{u}k) = \nabla \cdot \left[D\left(\nu + \frac{\nu_t}{\sigma_k}\right)\nabla k\right] + D\left(P_s + C_{fk}P_v - \epsilon\right) \tag{14}$$

$$\frac{\partial D\epsilon}{\partial t} + \nabla \cdot (D\mathbf{u}\epsilon) = \nabla \cdot \left[D\left(\nu + \frac{\nu_t}{\sigma_\epsilon}\right)\nabla \epsilon\right] + \frac{\epsilon}{k}D\left(C_{1\epsilon}\left(P_s + C_{f\epsilon}P_v\right) - C_{2\epsilon}\epsilon\right) \tag{15}$$

where $\sigma_k, \sigma_\epsilon, C_{1\epsilon}, C_{2\epsilon}, C_\mu$ are empirical coefficients (Rodi, 1987).

$$\sigma_k = 1.0, \quad \sigma\epsilon = 1.3, \quad C_{1\epsilon} = 1.44, \quad C_{2\epsilon} = 1.92, \quad C_\mu = 0.09 \tag{16}$$

P_s is shear production and described as

$$P_s = -\overline{u'_i u'_j}\frac{\partial u_i}{\partial x_j^*} \tag{17}$$

in which the Reynolds stress $\overline{u'_i u'_j}$ is calculated by a nonlinear model proposed by Lin and Liu (1998a,b) for breaking waves, which is given by

$$\begin{aligned} \overline{u'_i u'_j} =\ & -C_d k^2 \epsilon \left(\frac{\partial u_i}{\partial x_j^*} + \frac{\partial u_j}{\partial x_i^*}\right) + \frac{2}{3}k\delta_{ij} \\ & -C_1 \frac{k^3}{\epsilon 2}\left(\frac{\partial u_i}{\partial x_l^*}\frac{\partial u_l}{\partial x_j^*} + \frac{\partial u_j}{\partial x_l^*}\frac{\partial u_l}{\partial x_i^*} - \frac{2}{3}\frac{\partial u_l}{lx_k^*}\frac{\partial u_k}{\partial x_l^*}\delta_{ij}\right) \\ & -C_2 \frac{k^3}{\epsilon 2}\left(\frac{\partial u_i}{\partial x_k^*}\frac{\partial u_j}{\partial x_k^*} - \frac{1}{3}\frac{\partial u_l}{\partial x_k^*}\frac{\partial u_l}{\partial x_k^*}\delta_{ij}\right) \\ & -C_3 \frac{k^3}{\epsilon 2}\left(\frac{\partial u_k}{\partial x_i^*}\frac{\partial u_k}{\partial x_j^*} - \frac{1}{3}\frac{\partial u_l}{\partial x_k^*}\frac{\partial u_l}{\partial x_k^*}\delta_{ij}\right) \end{aligned} \tag{18}$$

where C_d, C_1, C_2, and C_3 are empirical coefficients as given by Lin and Liu (1998a,b).

$$\begin{aligned} C_d &= \frac{2}{3}\left(\frac{1}{7.4 + 2S_{max}}\right), \quad C_1 = \frac{1}{185.2 + 3D_{max}^2} \\ C_2 &= -\frac{1}{58.5 + 2D_{max}^2}, \quad C_3 = \frac{1}{370.4 + 3D_{max}^2} \end{aligned} \tag{19}$$

where

$$\begin{aligned} S_{max} &= k\epsilon \max\left\{\left|\frac{\partial u_i}{\partial x_i^*}\right|(\text{indices not summed})\right\} \\ D_{max} &= k\epsilon \max\left\{\left|\frac{\partial u_i}{\partial x_j^*}\right|\right\} \end{aligned} \tag{20}$$

The above coefficients may ensure the non-negativity of turbulent velocities and bounded Reynolds stress. They have been successfully applied to study breaking waves on plane beaches (Lin and Liu, 1998a,b). P_v is the turbulence production due to vegetation, which is formulated as follows by only considering drag force.

$$P_v = u_i f_{vi} = \frac{1}{2}C_D \lambda |\mathbf{u}|^3 \tag{21}$$

The drag-related coefficients C_{fk} and C_f in equations (Kobayashi et al., 1993) and (Li and Yan, 2007) deserve more discussion. Shimizu and Tsujimoto (1994) chose values of $C_{fk} = 0.07$ and $C_f = 0.16$ based on calibration. Lopez and Garcia (1998) discussed them based

on a theoretical argument, and suggested that the weighing coefficient C_{fk} should be set to unity if the total turbulence kinetic energy is to be modeled. The coefficient C_f is related to Cfk by $C_{f\epsilon} = C_{2\epsilon}/C_{1\epsilon}C_{fk} = 1.33$.

4. Numerical method

The numerical method of the current model follows the framework of NHWAVE (Ma et al., 2012). The well-balanced continuity and momentum equations (Gottlieb et al., 2001) and (Harten et al., 1983) are discretized by a combined finite-volume and finite-difference approach with a second-order Godunov-type scheme. The fluxes at cell faces are estimated by the HLL approximate Riemann solver (Harten et al., 1983). The two-stage second-order nonlinear Strong Stability-Preserving (SSP) Runge–Kutta scheme (Gottlieb et al., 2001) is adopted for time stepping in order to obtain second-order temporal accuracy. The advection and horizontal diffusion terms are treated explicitly, while the vertical diffusion is discretized implicitly. The Poisson equation is solved by a preconditioned GMRES solver using the high performance preconditioner HYPRE software library (http://acts.nersc.gov/hypre). The model is fully parallelized using the Message Passing Interface (MPI) with non-blocking communication.

To solve the equations, boundary conditions are required for all the physical boundaries. At the free surface, we have

$$\frac{\partial u}{\partial \sigma}\Big|_{\sigma=1} = \frac{\partial v}{\partial \sigma}\Big|_{\sigma=1} = 0, \quad w|_{\sigma=1} = \frac{\partial \eta}{\partial t} + u\frac{\partial \eta}{\partial x} + v\frac{\partial \eta}{\partial y}. \tag{22}$$

Dynamic pressure is zero at the free surface. For the $k - \epsilon$ model, zero gradients of k and are imposed.

$$\frac{\partial k}{\partial \sigma}\Big|_{\sigma=1} = \frac{\partial \epsilon}{\partial \sigma}\Big|_{\sigma=1} = 0. \tag{23}$$

At the bottom, the normal velocity and the tangential stress are prescribed. The normal velocity w is imposed through the kinematic boundary condition.

$$w|_{\sigma=0} = -u\frac{\partial h}{\partial x} - v\frac{\partial h}{\partial y}. \tag{24}$$

For the horizontal velocities, bottom shear stresses are considered.

$$\nu_t \frac{\partial u}{\partial \sigma}\Big|_{\sigma=0} = DC_b|u_b|u_b \tag{25}$$

where C_b is the bed drag coefficient, which can be computed from the law of the wall for fully rough, turbulent flow as $C_b = 0.16[\ln(15\Delta z_1/k_s)]^{-2}$, $\Delta z_1 = D\Delta\sigma_1$ is the thickness of the cell above the bed, and k_s is the bottom roughness height. u_b is the velocity at the cell above the bed. The boundary conditions for k and ϵ become

$$k_b = \frac{u_*^2}{\sqrt{C_\mu}} \quad \epsilon_b = \frac{u_*^3}{\kappa z} \tag{26}$$

in which $u_* = \kappa|u_b|/[\ln(15\Delta z_1/k_s)]$ is the friction velocity, $\kappa = 0.41$ is the von Karman constant.

5. Unidirectional flow through submerged vegetation

The model is first calibrated and tested against fully developed open channel flow through submerged vegetation. Two test runs are conducted corresponding to the laboratory experiments (case R31 and R32) of Shimizu and Tsujimoto (1994), which have been widely used to validate vegetation models (Cui and Neary, 2008; Neary, 2003). For both cases, 2D simulations are conducted. The domain is discretized by 16 cells in the streamwise direction and 50 vertical layers. The grid size is $\Delta x = 0.02$ m. Periodic boundary

conditions are specified at the streamwise boundaries. The flow is driven by an external pressure gradient depending on the laboratory flow condition.

In the laboratory experiments, uniform flow conditions were carefully kept by adjusting a weir. Vegetation was modeled by wooden cylinders. Turbulence measurements were conducted at the center of individual cylinders. For case R31, the water depth was 6.31 cm and the vegetation height was 4.1 cm. The vegetation height and water depth ratio was 0.65. The vegetation density was 0.10 cm^{-1}. The Flow condition was adjusted to yield a depth-averaged velocity of $u_0 = 11.21$ cm/s and an energy gradient of 1.63×10^{-3}. In the numerical model, the drag coefficient is chosen to be $C_D = 1.2$. Fig. 1 shows the model-data comparisons of vertical distribution of mean flow and Reynolds stress, which are both normalized by u_0. The horizontal lines indicate the top of the vegetation canopy. As we can see, the model results are very sensitive to the weighting coefficient $C_{f\epsilon}$. If $C_{f\epsilon}$ is taken as 1.28, the comparisons between the measured and calculated velocity and Reynolds stress profiles show an excellent agreement. Flow in the vegetation layer is noticeably suppressed. The velocity profile has an inflection near the top of the vegetation canopy, where the maximum Reynolds stress is observed. The inflection of velocity profile and strong shear at the top of vegetation tend to develop Kelvin–Helmholtz (KH) instabilities (Ghisalberti and Nepf, 2002). Notice that there is a reversal of flow gradient $\partial u/\partial z$ in the lower part of the canopy in the measurement, which was also observed by Shi et al. (1995) as shown in Fig. 2 in their paper and known as the secondary flow maximum. This feature of the velocity profile within the vegetation field cannot be reproduced by a RANS model.

The sensitivity of the model results to the drag-related coefficient $C_{f\epsilon}$ was investigated. Three runs with different values of $C_{f\epsilon}$ were carried out. The results are also shown in Fig. 1. We can see that both the mean velocity profile and Reynolds stress distribution are very sensitive to the coefficient. For the flow profile, $C_{f\epsilon}$ mainly changes the velocities above the vegetation. It is because $C_{f\epsilon}$ directly affects the turbulent mixing in the water column. A larger value of $C_{f\epsilon}$ gives a larger turbulent dissipation rate ϵ and smaller turbulent mixing (Fig. 2), which eventually leads to smaller Reynolds stress in the vegetation layer (Fig. 1). The maximum turbulent dissipation occurs near the top of the vegetation canopy, where the maximum Reynolds stress is found. In this region, the turbulent dissipation rate is the most sensitive to $C_{f\epsilon}$. Sensitivity tests of the drag coefficient
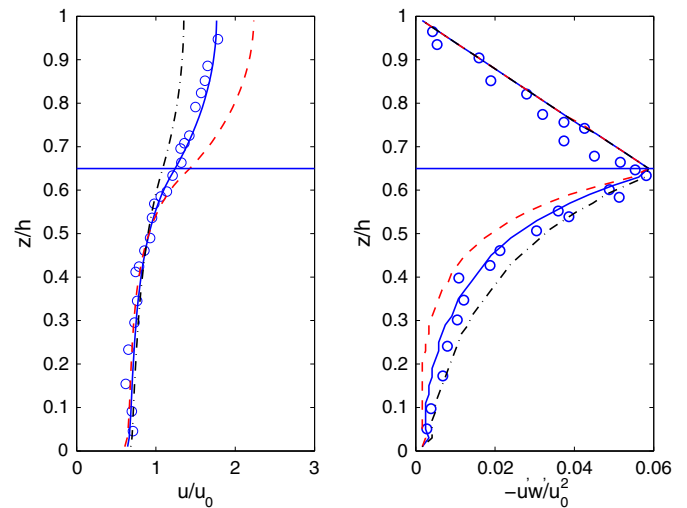

Fig. 1. Model-data comparisons of vertical distributions of mean flow (left panel) and Reynolds stress (right panel) for case R31. The vegetation height and water depth ratio is 0.650. z is the distance from the bottom. Solid line: $C_{f\epsilon=1.28}$; dashed line: $C_{f\epsilon} = C_{2\epsilon}/C_{1\epsilon}C_{fk}$; dash–dotted line: $C_{f\epsilon} = 1.20$; circles: measurements.
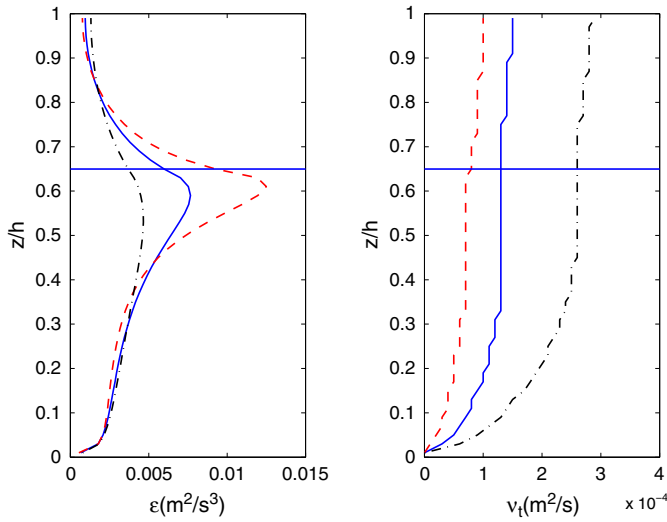
Fig. 2. Calculated vertical profiles of turbulent dissipate rate (left panel) and eddy viscosity (right panel) with different values of C_{f_ϵ}. Solid line: $C_{f_\epsilon=1.28}$; dashed line: $C_{f_\epsilon} = C_{2\epsilon}/C_{1\epsilon}C_{fk}$; dash–dotted line: $C_{f_\epsilon} = 1.20$.
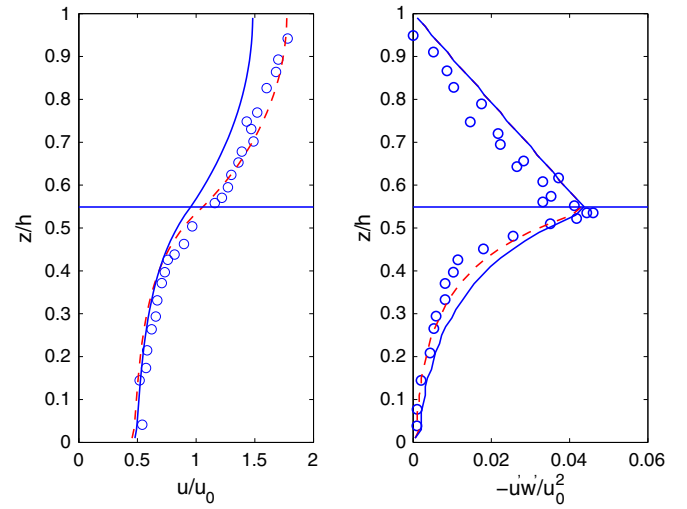

Fig. 4. Model-data comparisons of vertical distributions of mean flow (left panel) and Reynolds stress (right panel) for case R32. The vegetation height and water depth ratio is 0.55. Solid line: $C_{f_\epsilon=1.28}$; dashed line: $C_{f_\epsilon} = C_{2\epsilon}/C_{1\epsilon}C_{fk}$.

C_D were also conducted. The resulting velocity profiles and Reynolds stress distributions are shown in Fig. 3. The model results are not very sensitive to the drag coefficient, especially Reynolds stress. Increasing the drag coefficient reduces mean velocities slightly. However, the decrease of mean velocity is not significant as the drag coefficient is increased from 1.2 to 1.4.

For case R32, water depth was increased to be 7.47 cm. Therefore, the vegetation height and water depth ratio was 0.55. The vegetation density was kept as 0.10 cm^{-1}. The depth-averaged velocity of 13.87 cm/s and energy gradient of 2.13e−3 were specified. In the numerical model, the drag coefficient was still chosen as $C_D = 1.2$. Fig. 4 presents the model-data comparisons of mean velocity profile and Reynolds stress distribution. In this case, the theoretical value of $C_{f_\epsilon=1.33}$ gives the best comparisons with the laboratory measurements. As discussed above, C_{f_ϵ} determines turbulent mixing in the water column. As the vegetation height and water depth ratio decreases, vegetation effects on the water column become less significant, resulting in less turbulent mixing, which has to be modeled by a larger value of C_{f_ϵ}. These results demonstrate that C_{f_ϵ} is not a universal parameter. It varies with the vegetation height and water depth

ratio as well as with the flow characteristics. However, the theoretical value of C_{f_ϵ} can capture the main features of the flow in the vegetation regions. Therefore, it will be used in the following sections.

The turbulent kinetic energy (TKE) budget in the fully developed unidirectional flow over submerged vegetation is illustrated in Fig. 5, in which all the terms are normalized by the vegetation height h_v and depth-averaged velocity u_0. Near the top of the canopy, shear production P_s provides an important component of the TKE budget. The maximum shear production occurs at the top of the vegetation. Above the canopy, wake production P_v has no contribution to the TKE budget. The shear production of turbulence P_s is balanced by turbulent dissipation ϵ and turbulent transport T_t, which is similar to that in the boundary layer. Within the canopy, wake production due to vegetation P_v is the dominant source of turbulence. In the upper layer of the canopy ($z / h \geq 0.4$), shear production P_s is comparable to wake production P_v. This region corresponds to the "vertical exchange zone" (Nepf and Vivoni, 2000), where vertical turbulent exchange is dynamically important. In the lower layer of the canopy ($z / h \geq 0.4$), both shear production P_s and turbulent transport T_t are negligible. The vegetation-induced wake production P_v is simply
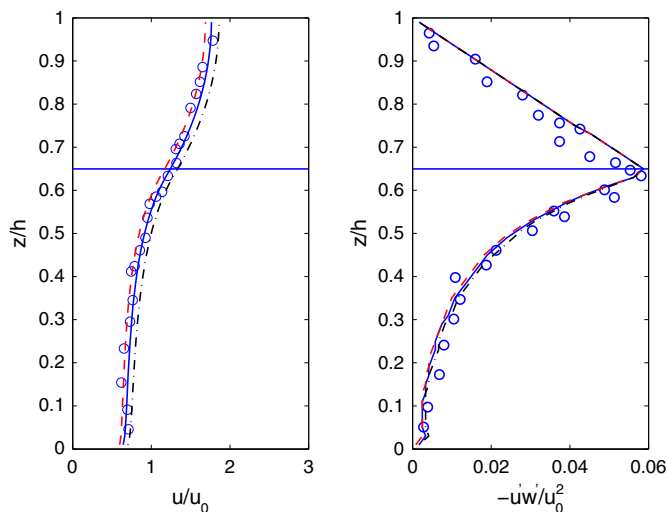

Fig. 3. Sensitivity of model results to drag coefficient C_D. Solid line: $C_D = 1.2$; dashed line: $C_D = 1.4$; dash–dotted line: $C_D = 1.0$.
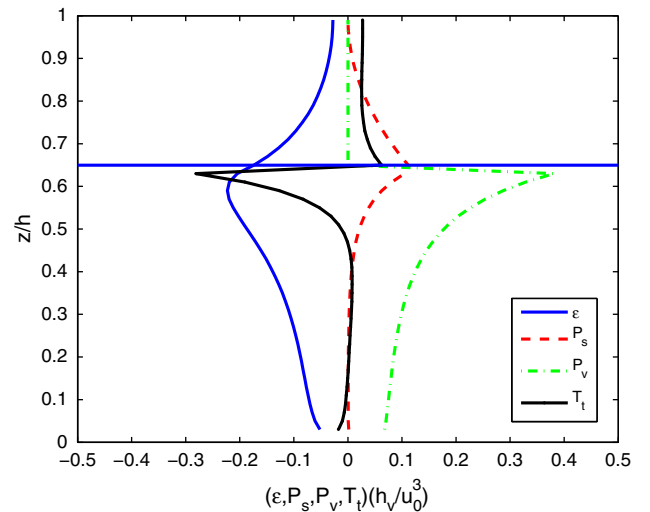

Fig. 5. Turbulent kinetic energy budget for case R31. Each term is normalized by the vegetation height h_v and depth-averaged velocity u_0. P_s is shear production; P_v is turbulence production due to vegetation; T_t is turbulent transport; ϵ is dissipation rate.

Table 1
Bulk drag coefficients for model runs, Section 6.

Case	$H_{\text{rms},0}$ (m)	T_p (s)	h (m)	C_D
IR5WD63	0.114	1.58	0.6	0.30
IR8WD57	0.15	2.53	0.5	0.12
IR12WD44	0.084	3.79	0.4	0.18
IR7WD68	0.131	2.21	0.6	0.18
IR6WD75	0.161	1.89	0.7	0.17
IR8WD104	0.187	2.53	1.0	0.10

balanced by turbulent dissipation ϵ, having $P_v \approx \epsilon$. This layer is called the "longitudinal exchange zone" (Nepf and Vivoni, 2000), where longitudinal advection is the dominant mechanism for momentum and turbulence exchange.

6. Nonbreaking random wave attenuation in vegetation field

In this section, the model is applied to study nonbreaking random wave attenuation through vegetation. The model results are compared with laboratory measurements by Dubi and Torum (1997), which have been used to validate several other models (Li and Zhang, 2010; Mendez and Losada, 2004; Suzuki et al., 2011). The experiments were conducted in a 33 m long, 0.5 m wide and 1.6 m high wave flume. Artificial kelp plants with an area per unit height of $b_v = 0.025$ m and a height of $h_v = 0.2$ m were used to model the submerged vegetation. The length of the vegetation field was $l_v = 9.3$ m. The number density of plants was $N = 1200$ m^{-2} m, such that the vegetation density was given by $\lambda = b_v N = 30$ m^{-1}. Experiments were carried out with varying water depths $h = 0.4 - 1.0$ m, wave peak periods $T_p = 1.26 - 4.42$ s and root-mean-square wave heights $H_{\text{rms}} = 0.045 - 0.17$ m. The incident irregular waves were generated using the Joint North Sea Wave Project (JONSWAP) spectrum with shape parameter $\gamma = 3.3$. Free surface elevations were measured by eight wave gauges spaced at 1 m intervals at $x = 1.15, \cdots, 8.15$ m, with $x = 0$ m located at the beginning of the vegetation field.

In the numerical model, the computational domain is 12.8 m long and is discretized by 640 cells with grid size $\Delta x = 0.02$ m. 20 vertical layers are used in all the simulations. Irregular waves are specified at the left boundary. A sponge layer with a width of 2.5 m is specified at the right boundary to avoid wave reflection. The drag-related coefficients in the $k-\epsilon$ turbulence model are taken as $C_{fk} = 1.0$ and $C_{f\epsilon} = C_{2\epsilon}/C_{1\epsilon}C_{fk}$. The drag coefficient C_D is case dependent. As discussed by Mendez and Losada (2004), the hydrodynamics, biomechanical properties and plant motion can all affect the bulk drag coefficient. Kobayashi et al. (1993) and Mendez and Losada (2004) found that the drag coefficient depends directly on the Reynolds number. Mendez and Losada (2004) found that the drag coefficient can be suitably correlated with the Keulegan–Carpenter number K, defined as $K = u_c T_p / b_v$, where u_c is a characteristic velocity acting on the plant and defined as the maximum horizontal velocity at the middle ($x = l_v/2$) and top of the vegetation field, as well as the relative height of the plants $\alpha = h_v/h$. In this study, the empirical formula given by Mendez and Losada (2004) is employed.

$$C_D = \frac{\exp(-0.0138Q)}{Q^{0.3}} \quad 7 \leq Q \leq 172 \tag{27}$$

where $Q = K/\alpha^{0.76}$ is a modified Keulegan–Carpenter parameter. The velocity u_c is defined using H_{rms} and T_p as the wave height and the wave period corresponding to a monochromatic wave train. The calculated bulk drag coefficients and wave conditions for all cases are given in Table 1. The root-mean-square wave height H_{rms} at a station is estimated by

$$H_{\text{rms}} = 2\sqrt{2}\sigma_\eta \tag{28}$$

where σ_η is the standard deviation of the free surface elevation. By calculating the wave heights for all the grid cells, the wave height distribution along the direction of wave propagation can be obtained. The comparisons of measured and calculated wave height distributions for 6 different cases are shown in Fig. 6. It is observed that the measured and calculated wave height distributions show excellent agreement, indicating that the model is capable of simulating wave attenuation through submerged vegetation.

Using Eq. (27), the bulk drag coefficient for case IR5WD63 is calculated as $C_D = 0.30$. In order to assess the sensitivity of wave
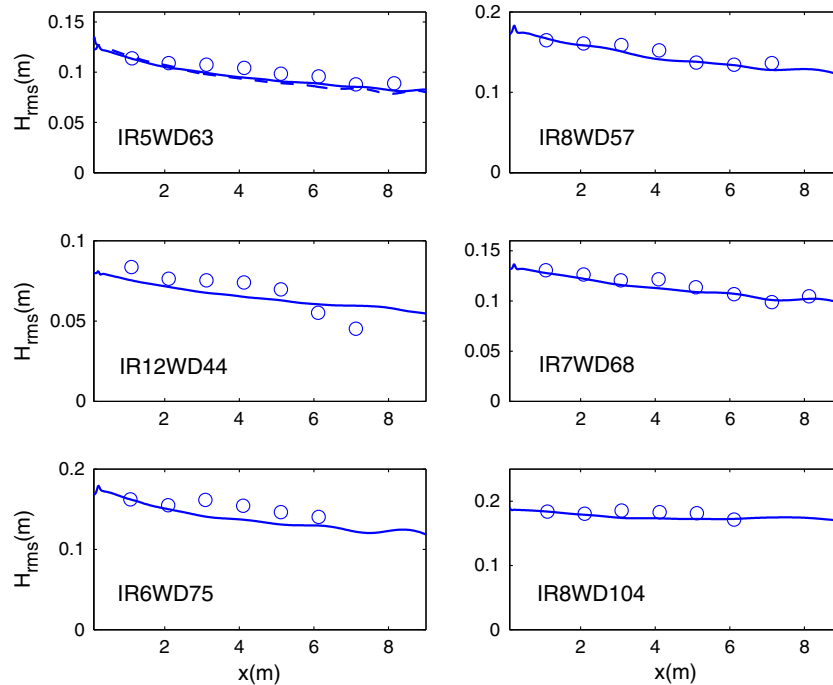

Fig. 6. Model-data comparisons of nonbreaking random wave attenuation over submerged vegetation. Solid line: simulations; circles: measurements by Dubi and Torum (1997).
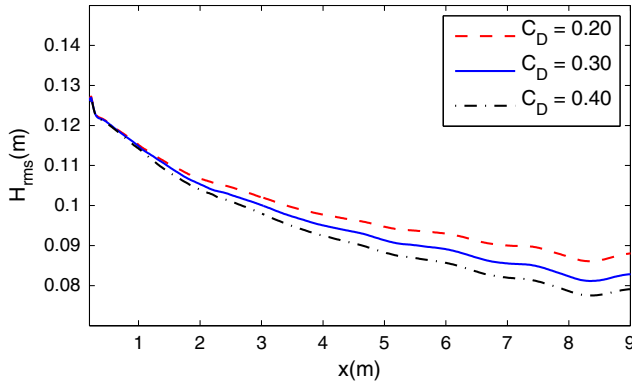
Fig. 7. Sensitivity tests of wave height distribution to bulk drag coefficients C_D for case IR5WD63. Solid Line: $C_D = 0.30$; dashed line: $C_D = 0.20$; dash–dotted line: $C_D = 0.40$.

attenuation over vegetation to the bulk drag coefficient C_D, another two simulations with $C_D = 0.20$ and $C_D = 0.40$ were conducted. The comparisons of these numerical results are shown in Fig. 7, which shows that the wave height distribution is sensitive to the drag coefficient, with a larger drag coefficient resulting in a larger wave attenuation rate. Sensitivity tests for coefficient $C_{f\epsilon}$ were also conducted. It was found that wave height evolution over vegetation is insensitive to this parameter, indicating that, for the prediction of wave height attenuation, the bulk drag coefficient C_D is the only parameter that has to be determined. Our numerical results show that, for a certain type of vegetation (Kelp in this case), the empirical formula of Mendez and Losada (2004) for drag coefficient works well.

Fig. 8 demonstrates the wave energy spectra of case IR5WD63 at two different locations ($x = 1.0$ m and 9.0 m) along the vegetation field. In order to see the vegetation effects on wave spectrum evolution, we also show the wave energy spectrum at $x = 9.0$ m without vegetation. Due to nonlinear wave energy transfer, high-frequency wave energy is decreased and low-frequency energy is increased across the vegetation field. However, the peak of the wave spectra stays around $f_p = 1 / T_p = 0.63$ Hz. The vegetation effects on wave energy spectrum evolution are significant. The wave energy all over the frequency band is dissipated by the vegetation canopy.

To see the vegetation effects on the velocity field, a simulation without vegetation was conducted. Fig. 9 shows the comparisons of
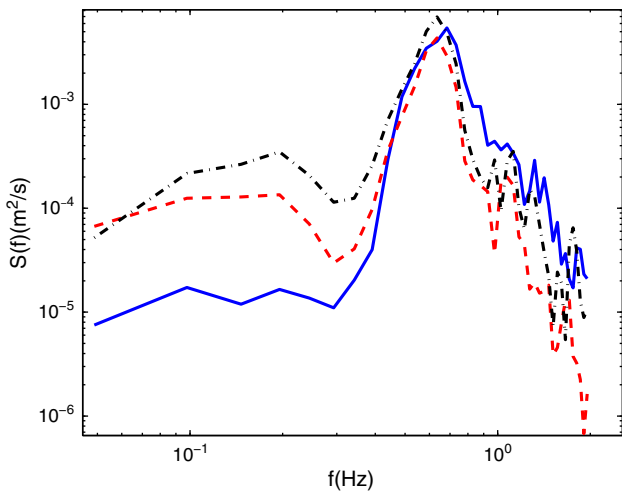

Fig. 8. Wave energy spectra for case IR5WD63 at $x = 1.0$ m (solid line) and $x = 9.0$ m (dashed line). The dash–dotted line shows the wave energy spectrum at $x = 9.0$ m without vegetation.
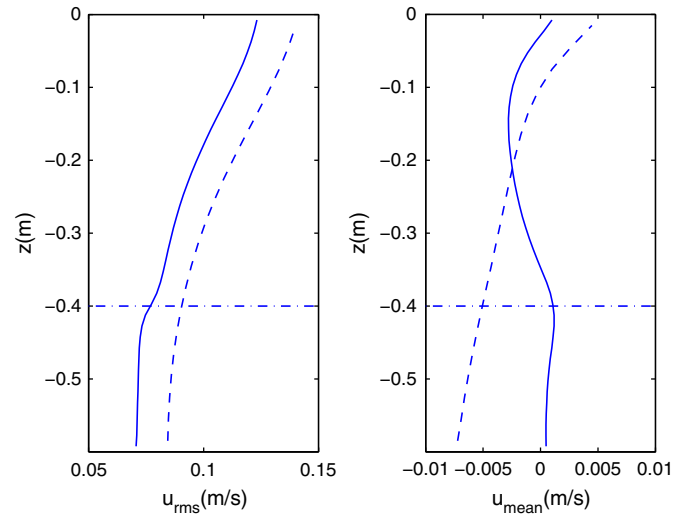

Fig. 9. Comparisons of root mean squared velocities (left panel) and Eulerian mean velocities (right panel) for case IR5WD63 at the center of vegetation field with (solid line) and without vegetation (dashed line). Dash–dotted line indicates the top of the vegetation.

root mean squared (rms) velocities and Eulerian mean velocities with and without vegetation. The root mean squared velocity is defined as

$$u_{\mathrm{rms}} = \sqrt{\frac{1}{T} \int_0^T u^2 dt} \qquad (29)$$

where T is the time used to estimate the room mean squared velocity. In this study $T = 50T_p$ is employed, T_p is the peak period of the JONSWAP spectrum. With the canopy resistance exerted on the flow, the root mean squared velocity is smaller within and near the top of the canopy than the free stream value. A wave boundary layer is developed at the top of the canopy where the vertical gradient of the horizontal velocity is large, as found by Lowe et al. (2005a,b) The vegetation effect on the Eulerian mean flow field is significant. Without vegetation, the Eulerian mean flow is in the direction of wave propagation near the surface and a return flow close to the bottom. With vegetation, however, the Eulerian mean flow is in the direction of wave propagation near the bottom, with the maximum value being found at the top of the vegetation canopy. Meanwhile, a return current is developed above the vegetation canopy. This phenomenon has been theoretically and experimentally studied by Luhar et al. (2010). They found that a mean current in the direction of wave propagation can be generated within the vegetation canopy even for purely oscillatory flow. This mean current is forced by nonzero wave stress, similar to the streaming observed in wave boundary layers.

7. Breaking random wave attenuation in vegetation field

In the nearshore, wave breaking is a crucial and complicated physical process that involves intense turbulence generation and bubble entrainment (Ma et al., 2011). Accurate simulation of wave breaking requires a sophisticated turbulence model capable of predicting the initiation of turbulence. The nonlinear $k-\epsilon$ model developed by Lin and Liu (1998a) has been proven to be a reliable tool for turbulence simulation under breaking waves in the surf zone. In this paper, the model is extended to include vegetation effects and will be validated in this section by using laboratory data of breaking random waves over submerged vegetation (Lovas and Torum, 2001).

The laboratory experiments were conducted in a 40 m long and 0.6 m wide wave flume. The vegetation plants were placed on a sandy 1:30 slope. The sand used in the experiment had a grain size
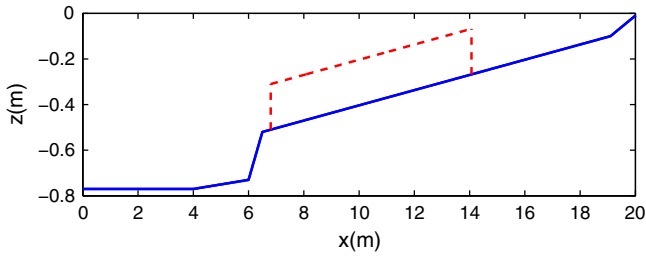
Fig. 10. Computational domain and water depth for Lovas and Torum (2001). The vegetation area is indicated by dashed lines.

of $D_{50} = 0.22$ mm. The length of the vegetation field was 7.27 m. The vegetation density was the same as that in the experiments of Dubi and Torum (1997), which was $\lambda = 30$ m^{-1}. The height of the individual plants was 0.2 m. For the numerical simulation, the computational domain and water depth are shown in Fig. 10, following Mendez and Losada (2004). The domain is discretized by 840 grid cells and 20 vertical layers. The grid size is $\Delta x = 0.025$ m. The incident irregular waves are based on the JONSWAP spectrum with shape parameter $\gamma = 3.3$. The bulk drag coefficients are calculated from Eq. (27). Three runs are carried out with varying incident significant wave heights and peak periods. Numerical results with and without kelp vegetation are compared. For each run, free surface elevations are collected at 10 wave gauges, the first defining the offshore wave conditions and the other nine being located along the sloping beach.

Fig. 11 shows the model-data comparisons of significant wave height evolution for three runs with and without kelp vegetation. The offshore water depth of these three cases is 0.77 m. The solid and dashed lines correspond to the numerical results with and without kelp. The crosses represent the experiment data for no kelp, and the circles, for the kelp cases. Without kelp, wave energy dissipation on the sloping beach is purely due to wave breaking, which is simulated by the nonlinear $k-\epsilon$ model. We can see that the model is capable of predicting wave shoaling and breaking. The location of the breaking

point is accurately captured by the model. The wave height decay after wave breaking is also reasonably predicted. With kelp, wave height on the sloping beach is much smaller, indicating that the vegetation effects on wave damping are not negligible. Because wave height is greatly reduced by vegetation, waves break closer to the shoreline. The dominant wave energy dissipation could be due to vegetation, rather than wave breaking.

Fig. 12 compares the wave-averaged Eulerian mean flow field with and without kelp vegetation for the case of $H_{mo} = 0.125$ m, $T_p = 3.5$ s. Without vegetation, wave breaking occurs around $x = 14.0$ m, from which significant shoreward mass transport is found near the surface and strong undertow is generated near the bottom. With vegetation, however, the Eulerian mean flow field is much more complicated. Due to vegetation-induced wave damping, waves break closer to the shoreline at around $x = 17.0$ m. We can see similar Eulerian flow pattern as that without vegetation after wave breaking, with shoreward flow near the surface and undertow close to the bottom. In the vegetated region, there is a thin layer near the top of the vegetation, which has a strong Eulerian mean current in the direction of wave propagation. It is similar to what was found in the previous section. This mean current is forced by nonzero wave stress as discussed by Luhar et al. (2010). To compensate this shoreward mean current, a strong mean flow in the offshore direction above the vegetation canopy is generated.

8. Waves propagating through a finite patch of vegetation

In this section, we investigate wave propagation through a finite patch of vegetation in the surf zone. A 3D simulation is conducted in a domain 14 m long and 12.8 m wide, discretized by 560×512 grid points. The wave tank consists of a beach with a slope of 0.03. The offshore water depth is 0.4 m. The incident wave is in the form of a cnoidal wave with a height of 0.1 m and a period of 2.0 s. The finite patch of vegetation covers an area 4 m long and 3.2 m wide as indicated by dashed lines in Fig. 13. The vegetation is rigid and emergent. To maximize the vegetation effects, the bulk drag coefficient C_D is chosen to be 0.5, which represents the upper range of
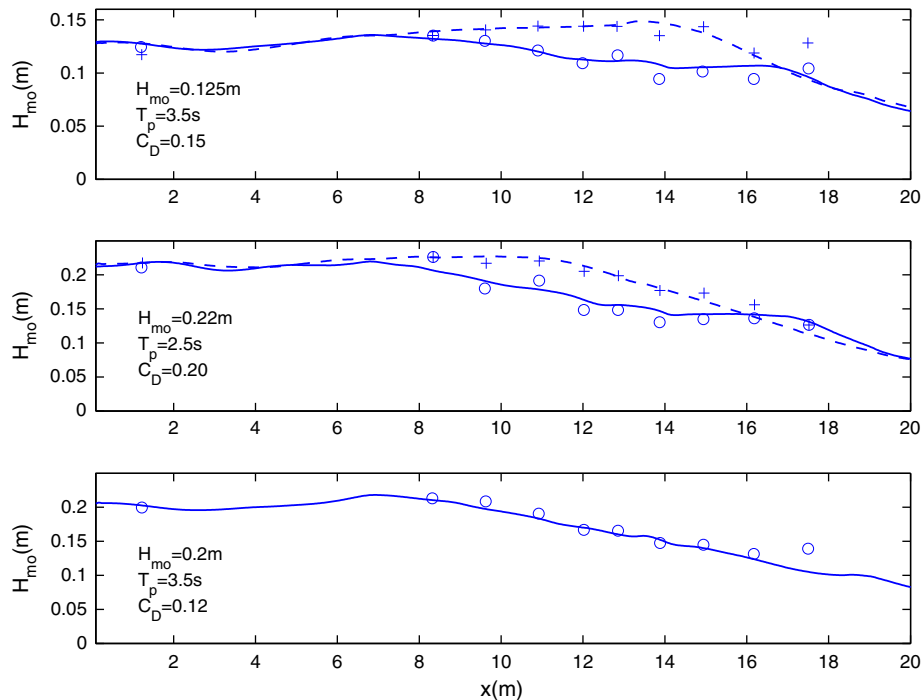

Fig. 11. Model-data comparisons of significant wave height distribution on a slope beach with and without vegetation. Solid line: kelp − model; dashed line: no kelp − model; circles: kelp − data; crosses: no kelp − data.
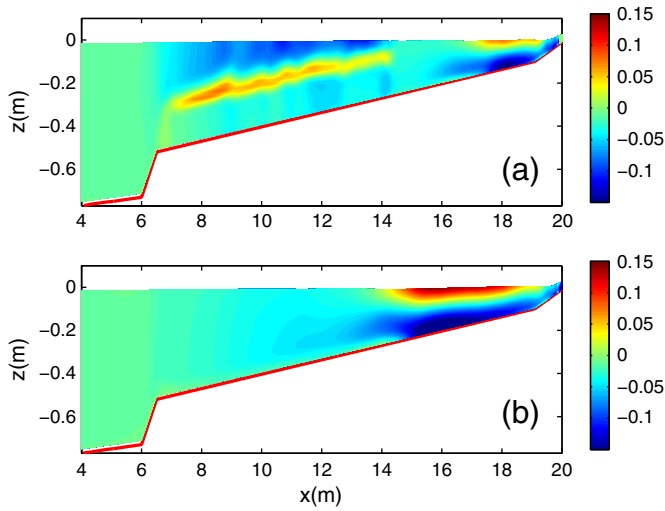
Fig. 12. The simulated wave-averaged Eulerian mean current for the case with $H_{mo} = 0.125$ m, $T_p = 3.5$ s. (a) with Kelp; (b) without Kelp. The units of the color bars are m/s.

Fig. 14. The wave height distribution averaged over 5 waves. The lower panel shows the cross-shore distributions of wave height at $y = 6.4$ m (solid line, vegetated zone) and $y = 3.2$ m (dashed line, unvegetated zone). The patch of vegetation is indicated by the dashed lines in the upper panel. The unit of the color bar is m.

values seen for the similarly scaled experimental data examined above. In the simulation, 20 vertical layers are employed. The $k-\epsilon$ turbulence model is used to simulate wave breaking and vegetation-induced turbulence.

Fig. 13 shows the simulated instantaneous surface elevation at 30 s. The lower panel of Fig. 13 compares the surface elevations at two cross-shore sections; one in the unvegetated zone and the other crossing the vegetated zone. Clearly, the wave height in the vegetated zone is attenuated more rapidly than in the adjacent unvegetated region, which is induced by the damping effects of the vegetation. Wave phase speed and wave length of the broken wave are also decreased in the vegetated region compared to the unvegetated region, which leads to refraction effects bending wave crests towards the patch in the exterior region. Fig. 14 shows the distribution of simulated wave height. The incident wave breaks at
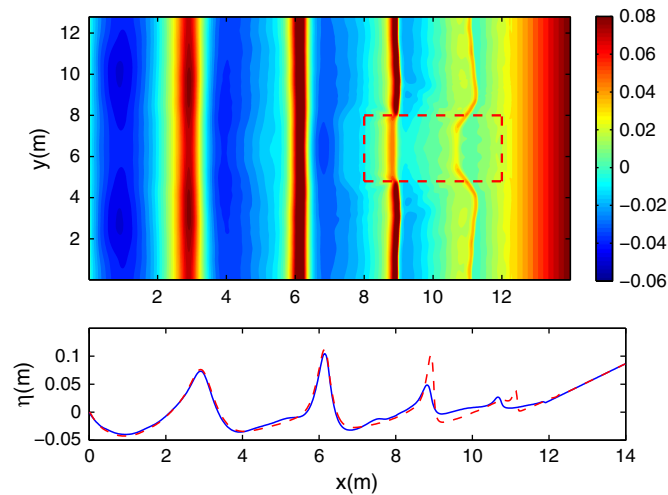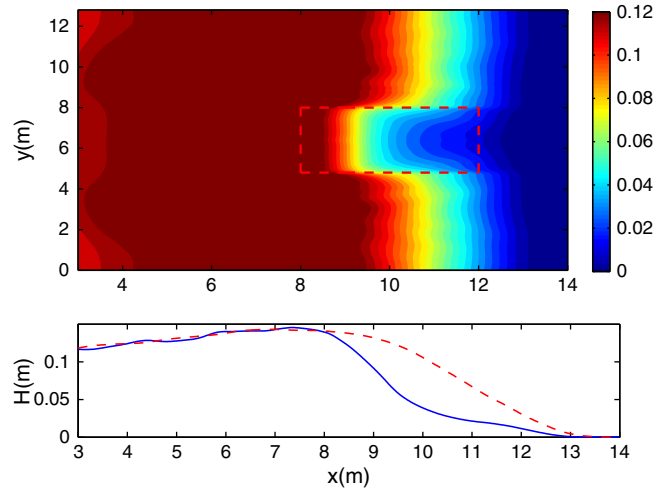

Fig. 13. The simulated instantaneous surface elevation at 20 s. The lower panel shows the cross-shore distributions of surface elevation at $y = 6.4$ m (solid line, vegetated zone) and $y = 3.2$ m (dashed line, unvegetated zone). The patch of vegetation is indicated by the dashed lines in the upper panel. The unit of the color bar is m.

around $x = 7.5$ m, which places the vegetation canopy entirely inside the surf zone. In the vegetated region, the wave height is greatly attenuated, which introduces alongshore variation of wave height in the surf zone, resulting in a nonuniform wave setup (Fig. 15) and near-shore circulation (Fig. 16). The cross-shore distribution of the wave setup is primarily determined by the cross-shore distribution of the wave height. Dean and Bender (2006) have studied the static wave setup affected by vegetation. There are two mechanisms that may induce or affect wave setup in the vegetation field; wave-forcing due to the cross-shore gradient of radiation stress, and gradient of momentum flux due to losses created by the vegetation. As shown in Fig. 14, at the offshore part of the vegetation ($8.0 < x < 10.0$ m), the cross-shore gradient of wave height in the vegetated zone is larger than that in the unvegetated zone, resulting in larger wave forcing. In this region, the wave forcing is dominant over the momentum loss due to vegetation, resulting in higher wave setup in the vegetated zone, relative to the unvegetated zone. At the onshore part of the vegetation ($10.0 < x < 12.0$ m), the cross-shore gradient of the wave height in the vegetated zone is smaller than that in the unvegetated zone. The momentum loss due to vegetation is dominant, resulting in a smaller wave setup in the vegetated zone compared to that in the unvegetated zone. The nonuniform alongshore distribution of the wave height and setup can induce nearshore circulation as displayed in Fig. 16, which shows the depth- and time-averaged flow field. It is anticipated that this nearshore circulation is primarily driven by the pressure gradient. Therefore, we plotted the distribution of longshore pressure gradient $\left(\frac{\partial \overline{\eta}}{\partial y}\right)$ in Fig. 17. In the inner part of the vegetation patch (close to the shoreline), the wave setup in the unvegetated zone is larger, producing strong longshore pressure gradients and convergence currents flowing into the vegetation patch. In the outer part of the vegetation patch (close to the breaker line), the wave setup in the vegetated zone is relatively larger, which generates divergence flows. The convergence/divergence flows create two large-scale vortices at the lateral edges of the vegetation patch. This flow pattern is similar to the rip current in the barred beach.

Fig. 18 demonstrates the wave-averaged Eulerian mean flow fields at two cross sections. One crosses the vegetated zone (section a), and the other crosses the unvegetated zone (section b). At section a, strong seaward mean flow is observed all over the water column. Due to the enhanced resistance within the vegetation, the mean
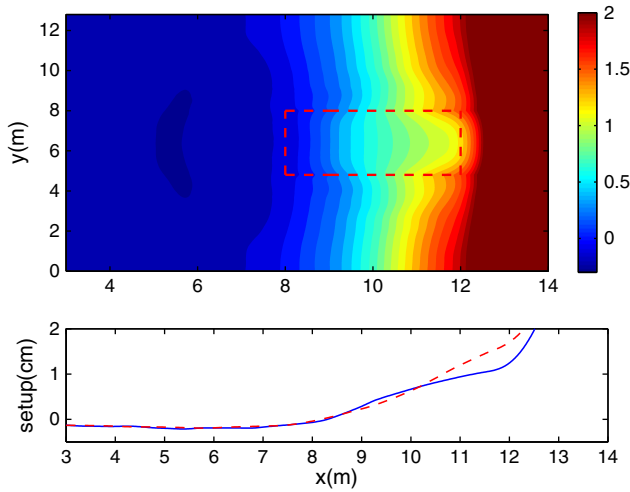
Fig. 15. The distribution of wave setup averaged over 5 waves. The lower panel shows the cross-shore distributions of wave setup at $y = 6.4$ m (solid line, vegetated zone) and $y = 3.2$ m (dashed line, unvegetated zone). The patch of vegetation is indicated by the dashed lines in the upper panel. The unit of the color bar is m.

Fig. 17. The distribution of longshore pressure gradient $\left(\frac{\partial \bar{\eta}}{\partial y}\right)$.

flow is noticeably reduced, relative to the unvegetated region. The strongest offshore mean flow is found to be located outside the vegetation patch. At section b, strong shoreward mean flow is observed inside the surf zone, with the maximum mean flow being located at the surface. Outside the surf zone, the mean flow is in the offshore direction. With the finite patch of vegetation, the offshore return flow acts like rip current in the vegetated zone. The nearshore circulation induced by vegetation canopy is anticipated to affect net sediment transport in the surf zone.

9. Conclusions

In this paper, a non-hydrostatic RANS model was developed to study turbulence, wave damping as well as nearshore circulation induced by aquatic vegetation. The model was based on an existing non-hydrostatic wave model (NHWAVE), which was initially developed by Ma et al. (2012). The nonlinear $k-\epsilon$ turbulence model proposed by Lin and Liu (1998a) was implemented into NHWAVE to simulate turbulent flow and wave breaking. Vegetation effects on the mean flow and turbulence were accounted for by ideally treating vegetation plants as rigid cylinders. Plant-induced profile drag force was considered,

while swaying motion and inertial forces were neglected. The model resulted in three additional parameters: bulk drag coefficient C_D as well as drag-related coefficients in the $k-\epsilon$ equations C_{fk} and $C_{f\epsilon}$. C_{fk} is theoretically taken as unity. The other two parameters C_D and $C_{f\epsilon}$ have to be determined empirically.

Although a number of assumptions have been made, the model was capable of simulating vegetated unidirectional flow as well as nonbreaking and breaking random wave attenuation induced by submerged vegetation with proper coefficients. It was found that $C_{f\epsilon}$ mainly affects turbulent mixing in the water column, with larger value of $C_{f\epsilon}$ resulting in weaker mixing. However, the main features of turbulent flow structures could be captured by choosing the theoretical value of $C_{f\epsilon} = C_{2\epsilon}/C_{1\epsilon}C_{fk}$. Wave attenuation in the vegetation field is insensitive to this parameter. However, it can be greatly affected by the bulk drag coefficient C_D. Using the empirical formula of Mendez and Losada (2004), the current model predicts vegetation-induced wave energy dissipation well.

Vegetation effects on nearshore circulation were also investigated. For submerged vegetation, a strong mean current may be generated near the top of the canopy due to nonzero wave stresses (Luhar et al., 2010). Wave propagation through a finite patch of vegetation was also investigated. The presence of a finite patch of vegetation can generate strong nearshore circulation and large-scale vortices at vegetation edges. The nearshore current converges in the vegetated
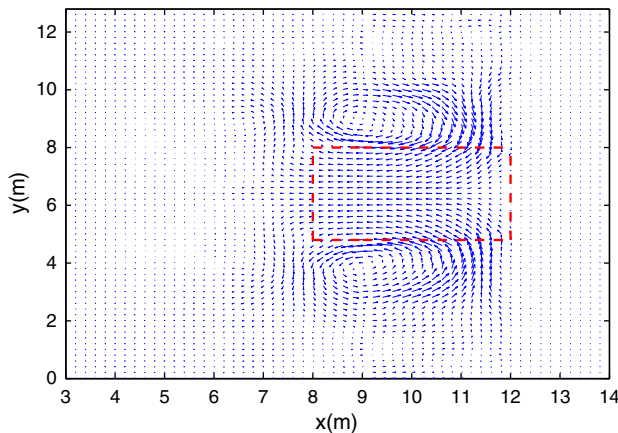

Fig. 16. The simulated depth- and time-averaged flow field with onshore current in the unvegetated zone and offshore current in the vegetated zone. The patch of vegetation is indicated by the dashed lines.
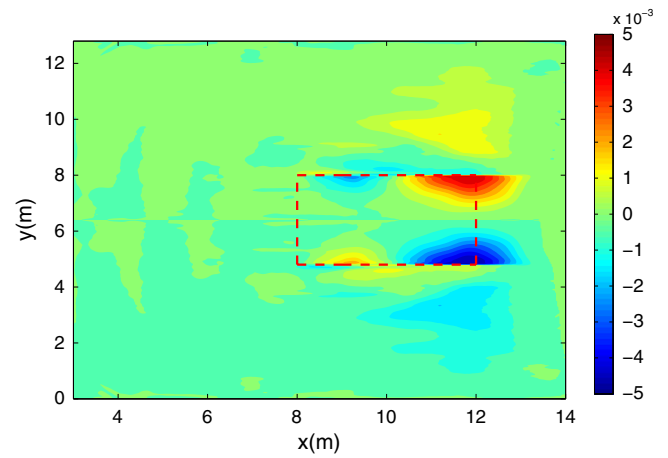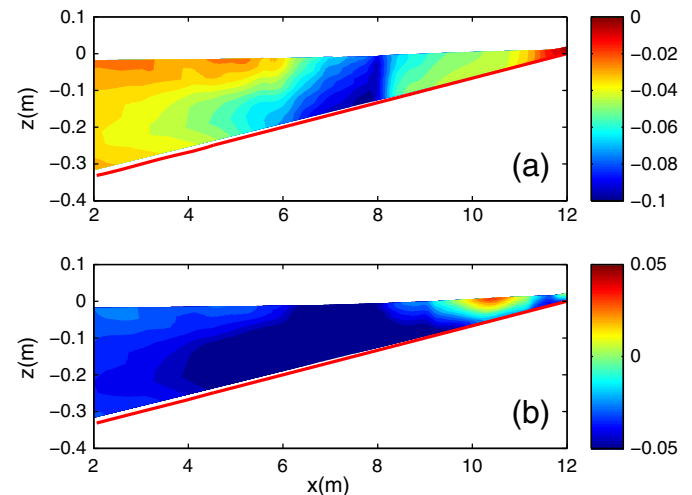

Fig. 18. The Eulerian mean flow field at two cross sections (a) $y = 6.4$ m (vegetated zone) and (b) $y = 3.2$ m (unvegetated zone). The units of the color bars are m/s.

zone and directs seaward. In the unvegetated zone, the mean flow is shoreward inside the surf zone. This nearshore circulation is primarily driven by the pressure gradient.

The current model treats vegetation as rigid cylinders, which cannot well represent the vegetation canopies in the field. In order to better simulate vegetation-induced wave damping and turbulence generation, it is necessary to take into account the flexibility of the vegetation. Our future work will be focused on incorporating flexible vegetation into the model.

Acknowledgments

References

Augustin, L.N., Irish, J.L., Lynett, P., 2009. Laboratory and numerical studies of wave damping by emergent and near-emergent wetland vegetation. Coastal Engineering 56, 332–340.
Ayotte, K.W., Finnigan, J.J., Raupach, M.R., 1999. A second-order closure for neutrally stratified vegetative canopy flows. Boundary-Layer Meteorology 90, 189–216.
Chen, Q., Zhao, H., 2012. Theoretical models for wave energy dissipation caused by vegetation. Journal of Engineering Mechanics 138, 221–229.
Cui, J., Neary, V.S., 2008. LES study of turbulent flows with submerged vegetation. Journal of Hydraulic Research 46, 307–316.
Dalrymple, R.A., Kirby, J.T., Hwang, P.A., 1984. Wave diffraction due to areas of energy dissipation. Journal of Waterway, Port, Coastal, and Ocean Engineering 110, 67–79.
Dean, R.G., Bender, C.J., 2006. Static wave setup with emphasis on damping effects by vegetation and bottom friction. Coastal Engineering 53, 149–156.
Dubi, A., Torum, A., 1997. Wave damping by kelp vegetation. In: Edge, B.L. (Ed.), Proc. 24th Coast. Eng. Conf. ASCE, New York, pp. 142–156.
Ghisalberti, M., Nepf, H.M., 2002. Mixing layers and coherent structures in vegetated aquatic flows. Journal of Geophysical Research 107, C2. http://dx.doi.org/10.1029/2001JC000871.
Gottlieb, S., Shu, C.-W., Tadmor, E., 2001. Strong stability-preserving high-order time discretization methods. SIAM Review 43, 89–112.
Harten, A., Lax, P., van Leer, B., 1983. On upstream differencing and Godunov-type schemes for hyperbolic conservation laws. SIAM Review 25, 35.
Jarvela, J., 2005. Effect of submerged flexible vegetation on flow structure and resistance. Journal of Hydrology 307, 233–241.
Kadlec, R., 1990. Overland flow in wetlands: vegetation resistance. Journal of Hydraulic Engineering 116, 691–707.
King, A.T., Tinoco, R.O., Cowen, E.A., 2012. A $k-\epsilon$ turbulence model based on the scales of vertical shear and stem wakes valid for emergent and submerged vegetated flows. Journal of Fluid Mechanics 701, 1–39.
Kobayashi, N., Raichle, A.W., Asano, T., 1993. Wave attenuation by vegetation. Journal of Waterway, Port, Coastal, and Ocean Engineering 119 (1), 30–48.
Li, C.W., Yan, K., 2007. Numerical investigation of wave–current–vegetation interaction. Journal of Hydraulic Engineering 133 (7), 794–803.
Li, C.W., Zhang, M.L., 2010. 3D modelling of hydrodynamics and mixing in a vegetation field under waves. Computer & Fluids 39, 604–614.
Liang, Q., Marche, F., 2009. Numerical resolution of well-balanced shallow water equations with complex source terms. Advances in Water Resources 32, 873–884.
Lin, P., Li, C.W., 2002. A σ-coordinate three-dimensional numerical model for surface wave propagation. International Journal for Numerical Methods in Fluids 38, 1045–1068.
Lin, P., Liu, P.L.-F., 1998a. A numerical study of breaking waves in the surf zone. Journal of Fluid Mechanics 359, 239–264.
Lin, P., Liu, P.L.-F., 1998b. Turbulence transport, vorticity dynamics, and solute mixing under plunging breaking waves in the surf zone. Journal of Geophysical Research 103, 15,677–15,694.
Loder, N.M., Cialone, M.A., Irish, J.L., Wamsley, T.V., 2009. Sensitivity of hurricane surge to morphological parameters of coastal wetlands. Estuarine, Coastal and Shelf Science 84 (4), 625–636.

Lopez, F., Garcia, M., 1998. Open-channel flow through simulated vegetation: suspended sediment transport modeling. Water Resources Research 34 (9), 2341–2352.
Lovas, S.M., Torum, A., 2001. Effect of the kelp Laminaria hyperborea upon sand dune erosion and water particle velocities. Coastal Engineering 44, 37–63.
Lowe, R.J., Koseff, J.R., Monismith, S.G., 2005a. Oscillatory flow through submerged canopies: 1. Velocity structure. Journal of Geophysical Research 110, C10016. http://dx.doi.org/10.1029/2004JC002788.
Lowe, R.J., Koseff, J.R., Monismith, S.G., 2005b. Oscillatory flow through submerged canopies: 2. Canopy mass transfer. Journal of Geophysical Research 110, C10017. http://dx.doi.org/10.1029/2004JC002789.
Luhar, M., Coutu, S., Infantes, E., Fox, S., Nepf, H., 2010. Wave-induced velocities inside a model seagrass bed. Journal of Geophysical Research 115, C12005. http://dx.doi.org/10.1029/2010JC006345.
Lynett, P., Wu, T.-R., Liu, P.L.-F., 2002. Modeling wave runup with depth-integrated equations. Coastal Engineering 46 (2), 89–107.
Ma, G., Shi, F., Kirby, J.T., 2011. A polydisperse two-fluid model for surf zone bubble simulation. Journal of Geophysical Research 116, C05010. http://dx.doi.org/10.1029/2010JC006667.
Ma, G., Shi, F., Kirby, J.T., 2012. Shock-capturing non-hydrostatic model for fully dispersive surface wave processes. Ocean Modelling 43–44, 22–35.
Mendez, F.J., Losada, I.J., 2004. An empirical model to estimate the propagation of random breaking and nonbreaking waves over vegetation fields. Coastal Engineering 51, 103–118.
Moller, I., Spencer, T., French, J.R., Leggett, D.J., Dixon, M., 1999. Wave transformation over salt marshes: a field and numerical modelling study from North Norfolk, England. Estuarine, Coastal and Shelf Science 49, 411–426.
Neary, V.S., 2003. Numerical solution of fully-developed flow with vegetative resistance. Journal of Engineering Mechanics 129 (5), 558–564.
Nepf, H.M., 1999. Drag, turbulence, and diffusion in flow through emergent vegetation. Water Resources Research 35 (2), 479–489.
Nepf, H.M., Ghisalberti, M., 2008. Flow and transport in channels with submerged vegetation. Acta Geophysica 56 (3), 753–777.
Nepf, H.M., Vivoni, E.R., 2000. Flow structure in depth-limited, vegetated flow. Journal of Geophysical Research 105 (C12), 28,547–28,557.
Raupach, M.R., Shaw, R.H., 1982. Averaging procedures for flow within vegetation canopies. Boundary-Layer Meteorology 22, 79–90.
Rodi, W., 1987. Examples of calculation methods for flow and mixing in stratified flows. Journal of Geophysical Research 92 (5), 5305–5328.
Schultz, M., Kozerski, H.-P., Pluntke, T., Rinke, K., 2002. The influence of macrophytes on sedimentation and nutrient retention in the lower river spree. Water Resources Research 37, 569–578.
Sheng, Y.P., Lapetina, A., Ma, G., 2012. The reduction of storm surge by vegetation canopies — three-dimensional simulations. Geophysical Research Letters 39, L20601. http://dx.doi.org/10.1029/2012GL053577.
Shi, Z., Pethick, J., Pye, K., 1995. Flow structure in and above the various heights of a salt marsh canopy: a laboratory flume study. Journal of Coastal Research 11, 1204–1209.
Shields, F.D., Rigby, J.R., 2005. River habitat quality from river velocities measured using acoustic Doppler current profiler. Environmental Management 36 (4), 565–575.
Shimizu, Y., Tsujimoto, T., 1994. Numerical analysis of turbulent open-channel flow over a vegetation layer using a $k-\epsilon$ turbulence model. Journal of Hydroscience and Hydraulic Engineering 11 (2), 57–67.
Spalart, P.R., Allmaras, S.R., 1994. A one-equation turbulence model for aerodynamic flows. La Recherche Aérospatiale 1, 5–21.
Stelling, G., Zijlema, M., 2003. An accurate and efficient finite-difference algorithm for non-hydrostatic free-surface flow with application to wave propagation. International Journal for Numerical Methods in Fluids 43, 1–23.
Suzuki, T., Zijlema, M., Burger, B., Meijer, M.C., Narayan, S., 2011. Wave dissipation by vegetation with layer schematization in SWAN. Coastal Engineering 59 (1), 64–71.
Tsujimoto, T., 2000. Fluvial processes in streams with vegetation. Journal of Hydraulic Research 37, 789–804.
Wamsley, T.V., Cialone, M.A., Smith, J.M., Atkinson, J.H., Rosati, J.D., 2010. The potential of wetlands in reducing storm surge. Ocean Engineering 37, 59–68.
Wilcock, R., Champion, P., Nagels, J., Crocker, G., 1999. The influence of aquatic macrophytes on the hydraulic and physicochemical properties of a New Zealand lowland stream. Hydrobiologia 416 (1), 203–214.
Wu, F.-C., Shen, H.-W., Chou, Y.-J., 1999. Variation of roughness coefficients for unsubmerged and submerged vegetation. Journal of Hydraulic Engineering 125 (9), 934–942.
Zong, L., Nepf, H., 2010. Flow and deposition in and around a finite patch of vegetation. Geomorphology 116, 363–372.
Zong, L., Nepf, H., 2011. Spatial distribution of deposition within a patch of vegetation. Water Resources Research 47, W03516. http://dx.doi.org/10.1029/2010WR009516.